Catalysis Today 144 (2009) 69–74

Contents lists available at ScienceDirect

Catalysis Today

journal homepage: www.elsevier.com/locate/cattod

Photocatalytic hydrogen production by liquid- and gas-phase reforming of CH_3OH over flame-made TiO_2 and Au/TiO_2

Gian Luca Chiarello, Lucio Forni, Elena Selli *

Dipartimento di Chimica Fisica ed Elettrochimica, CIMAINA and ISTM-CNR, Università degli Studi di Milano, Via Golgi 19, I-20133 Milano, Italy

ARTICLE INFO

Article history:
Available online 10 February 2009

Keywords:
Photocatalytic H_2 production
Methanol photoreforming
Flame spray pyrolysis
Au/TiO_2

ABSTRACT

TiO_2 and 1% Au/TiO_2 powders, synthesised by flame spray pyrolysis and possessing high specific surface area (106 $m^2\ g^{-1}$) and anatase content (*ca.* 90%), were tested as photocatalysts in hydrogen production from methanol photoreforming, employing a closed recirculation apparatus. The irradiated photoreactor consisted either in a quartz vessel containing an aqueous suspension of the photocatalyst, or in a newly set-up Plexiglas cell, containing the same amount of catalyst immobilised on quartz grains, which was continuously fed with methanol/water vapours. The gas-phase composition during irradiation was analysed by gas chromatography and quadrupolar mass spectrometry, which allowed the identification of formaldehyde as the only intermediate species. The photocatalytic activity of the flame-made materials was higher than that of commercial Degussa P25 TiO_2 and of 1% Au/P25 obtained *via* deposition of preformed gold nanoparticles on P25. In particular, a 30 times higher photocatalytic hydrogen production was obtained upon gold addition to TiO_2. Furthermore, a 30% higher reaction rate was attained with the vapour phase reactor, *i.e.* in the absence of liquid-phase mass transfer rate limitations, ensuring the production of up to 10.2 mmol of $H_2\ h^{-1}\ g_{cat}^{-1}$, with an apparent photon efficiency of 6.3%.

1. Introduction

The increase of pollutants emissions consequent to the raise of world energy demand, up to now mainly based on fossil fuels exploitation, urgently requires the development of alternative, environmentally friendly energy sources. The photocatalytic production of hydrogen over semiconductor metal oxides represents a promising way to convert solar into chemical energy at ambient temperature and pressure, in the form of a clean energy vector. Hydrogen can be produced either by water photosplitting [1,2] or, even more efficiently, by photoinduced reforming of organic compounds, including methane [3], alcohols [4–9], aldehydes [6,8] and organic acids [6,10], to yield H_2 and CO_2 mixtures. The latter process may also be envisaged as an effective way to combine the abatement of organic wastewater pollutants with hydrogen production in an efficient and low cost single step.

Different semiconductors, mainly consisting of rather complex mixed metal oxides, have been proposed as photocatalysts for these reactions in recent years [11–14]. However, titanium dioxide modified by noble metals deposition has widely been proved to be one of the best photocatalysts for hydrogen production, mainly for its ability to enhance photoproduced electron–hole pair separation and photoinduced reduction processes [15]. Indeed, as the Fermi level of the noble metal is lower in energy than the conduction band of TiO_2, photopromoted electrons can efficiently migrate and be captured by the metal, whereas the holes remain in the TiO_2 valence band [16]. The rate of photocatalytic hydrogen production further increases in the presence of organic compounds able to satisfactorily scavenge valence band holes and undergo relatively rapid and irreversible oxidation.

Traditional methods of noble metal deposition on solid catalysts usually require several steps and invariantly imply the loss of a certain fraction of noble metal. We recently showed [9] that very active, high surface area titanium dioxide-based photocatalysts, also containing noble metal nanoparticles, can be synthesised in a single step by flame spray pyrolysis (FP) [17]. Furthermore, the physico-chemical properties of the so produced photocatalytic materials can be easily tuned up by properly adjusting the parameters and conditions adopted in their preparation.

Preliminary photocatalytic tests of such materials involved hydrogen evolution from illuminated aqueous suspensions, as usually found in the literature. This *modus operandi*, however, evidenced mass transfer limitations to hydrogen production and short-time stability of the suspensions [9]. An alternative setup has thus been adopted in the present work to test the photocatalytic

* Corresponding author. Tel.: +39 02 503 14237; fax: +39 02 503 14300.
E-mail address: elena.selli@unimi.it (E. Selli).

0920-5861/$ – see front matter © 2009 Elsevier B.V. All rights reserved.
doi:10.1016/j.cattod.2009.01.023

activity of flame-made materials in the steam photoreforming of volatile organic compounds, implying catalysts immobilisation on a bed of quartz grains, which were continuously fed with methanol/water vapours. This system allowed a much more accurate control of the reaction conditions and led to an increase of both hydrogen production rate and overall photon efficiency. The newly set-up photocatalytic system thus appears very promising for H_2 production, *e.g.* to feed fuel cells, also because no CO and formic acid were detected as intermediate species in the gas phase.

2. Experimental

2.1. Photocatalysts preparation

TiO_2 and 1% Au/TiO_2 were synthesised in a single step by the FP method as already described [17], starting from 0.15 M titanium(IV)-isopropoxide xylene solutions, also containing the required amount of gold precursor (dimethyl-gold(III)-acetylacetonate), when necessary. The so obtained liquid organic solution was fed at 3.1 mL min^{-1} by a syringe pump into the flame reactor [17] and dispersed by oxygen (6 L min^{-1}) at 1.5 bar constant pressure drop across the burner nozzle. The spray was ignited by a methane/oxygen flame ring surrounding the central nozzle, forming the main vertical flame. The produced powders were collected on a glass fibre filter (Whatman GF/A, 26 cm in diameter) placed on a cylindrical steel vessel surmounting the flame reactor.

Degussa P25 TiO_2 was employed as received. The Au/P25 sample was prepared by depositing *tetrakis*(hydroxymethyl)phosphonium chloride (THPC)-stabilised gold nanoparticles on Degussa P25 TiO_2, as detailed elsewhere [18], and contained the same amount of gold (1 wt.%) as FP-made Au/TiO_2. Briefly, a brown metallic sol was generated by adding a 0.05 M THPC aqueous solution to a 10^{-3} M NaOH solution, followed by a dropwise addition of 10^{-3} M $HAuCl_4$. The stabilised Au nanoparticles were immobilised on TiO_2 by simply dipping the oxide in the metal dispersion, which was acidified at pH 1.5–2 by H_2SO_4 addition. The slurry was then filtered and the photocatalyst was thoroughly washed with distilled water and dried at 100 °C for 2 h.

2.2. Photocatalysts characterisation

The BET specific surface area was measured by N_2 adsorption/desorption at 77 K on a Micromeritics ASAP 2010 apparatus, after out-gassing *in vacuo* at 300 °C for at least 6 h. X-ray diffraction patterns were recorded on a Philips PW3020 powder diffractometer, by using the Cu Kα radiation (λ = 1.54056 Å) and compared with literature data [19] for phase recognition. Quantitative phase analysis was made by the Rietveld refinement method [20], using the "Quanto" software [21]. UV–vis diffuse reflectance was measured by a Perkin-Elmer Lambda 35 apparatus equipped with an integration sphere (Labsphere RSA-PE-20).

For high-resolution transmission electron microscopy (HRTEM) and scanning transmission electron microscopy (STEM), the material was dispersed in ethanol and deposited onto a perforated carbon foil, supported on a copper grid. The analysis was done on a Tecnai F30 microscope (FEI, Eindhoven; field emission cathode) operated at 300 kV.

2.3. Photocatalytic tests

The photocatalytic activity in hydrogen production was tested either (i) with the photocatalyst powder (14 mg) dispersed in 6 vol.% CH_3OH/H_2O suspension contained in a 45 mL quartz vessel (suspension reactor) or (ii) with the same amount of photocatalyst deposited on quartz grains (vapour phase reactor). The so obtained photocatalyst bed was continuously fed with methanol/water vapours. Both photoreactors were connected to a closed stainless steel system, where the gas phase was continuously recirculated at constant rate. The whole setup equipped with the suspension reactor is fully described in Ref. [9].

The sketch of the laboratory scale apparatus equipped with the vapour phase reactor is shown in Fig. 1. The photoreactor consisted in a flat cylindrical Plexiglas cell (A), having a central 2 mm thick round hollow (B), where the photocatalyst bed was placed. This was prepared by mixing, on a Petri dish, 14 mg of photocatalyst with 3 g of 20–40 mesh (0.42–0.85 mm) quartz beads, and a few droplets of distilled water, followed by drying at 70 °C for 6 h. The

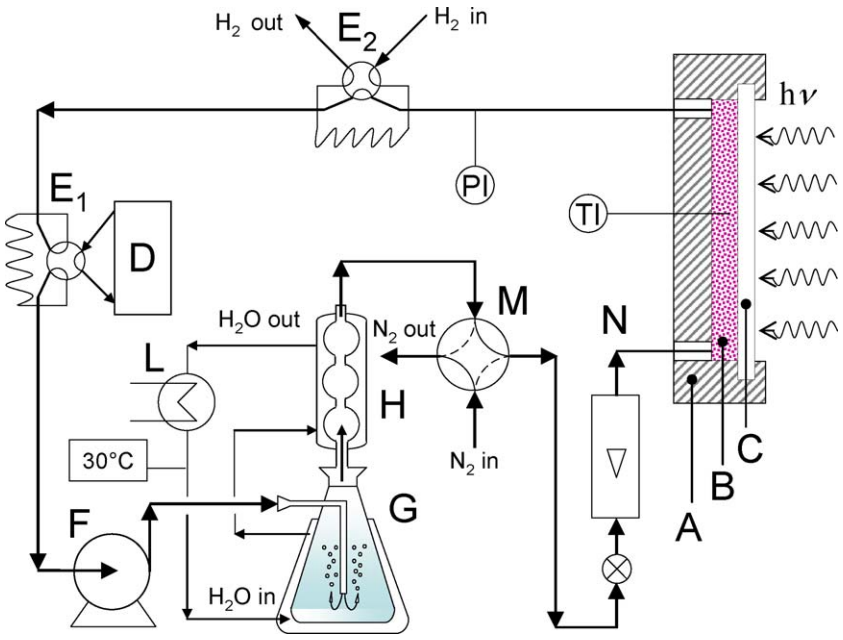

Fig. 1. Sketch of the experimental setup for vapour phase photocatalytic activity measurements: (A) Plexiglas photoreactor; (B) photocatalyst bed; (C) Pyrex-glass window; (D) detector (gas chromatograph with TC or quadrupolar mass spectrometer, QMS); (E_1, E_2) six ways sampling valves; (F) bellow pump; (G) thermostated bubbler; (H) refrigerator-condenser; (M) four ways ball valve (dotted line: position for pre-flushing with inert gas; solid line: position for gas-phase recirculation); (L) thermostat; (N) gas flow meter; TI and PI: temperature and pressure indicators.

opposite face of the cell hosted a Pyrex-glass 20 cm^2 round window (C), through which the bed was irradiated. During irradiation, the reactor temperature was 55 ± 5 °C, as continuously monitored by means of a thermocouple (TI) placed inside the cell. The absolute pressure was 1.2 bar at the beginning of the runs and slightly increased during irradiation, as a consequence of hydrogen accumulation in the gas phase. The reactor was inserted in the recirculation stainless steel system, initially containing an inert gas (usually nitrogen), which was forced at the desired flow rate (typically 40 mL min^{-1}) by means of a bellow pump (Metal Bellows, MB41E) (F), to pass through a bubbling system (G) surmounted by a refrigerator-condenser (H), both maintained at 30 °C by an external thermostatic water recirculation system. The bubbler reservoir was filled with a 20 vol.% MeOH aqueous solution, corresponding to 0.1 mole fraction of methanol in water. The outlet gas was therefore N_2 saturated by $MeOH/H_2O$ vapours at 30 °C. The so obtained gas mixture was finally fed to the catalyst bed in the photoreactor. Prior to any run, the whole setup was thoroughly flushed with inert gas in the dark, in order to remove any trace of oxygen.

With both types of photoreactor, the amount of hydrogen produced under irradiation and accumulated in the inert gas was determined on line, by sampling the recirculating gas phase by means of the six ways valve E_1 and injecting 1.0 mL samples into a gas chromatograph (GC, Agilent 6890N) equipped with a molecular sieve column (MolSieve 5A) and TC detector (D). N_2 was employed as carrier gas. The GC response was first calibrated by injecting known volumes of H_2 into the recirculation system through the six ways sampling valve E_2 (Fig. 1).

In some of the runs carried out by employing the vapour phase reactor, the six ways valve E_1 was connected to a quadrupolar mass spectrometer (QMS) (MKS, PPT Residual Gas Analyser). In this case the recirculation system was thoroughly flushed with pure He before starting irradiation. The composition of the recirculating gas phase during irradiation was determined by successively injecting 1.0 mL aliquots into the QMS system. For quantitative analysis, the QMS detector was preliminarily calibrated by injecting $H_2/CO_2/He$ mixtures with different percent composition in the He carrier gas stream and by plotting the peak areas of the mass to charge ratio (m/z) signals (2 for H_2 and 44 for CO_2) *vs.* the H_2 and CO_2 percent concentration in the injected mixtures.

The irradiation source was an iron halogenide mercury arc lamp (Jelosil, 250 W), placed at 20 cm from the reactor, emitting in the 330–450 nm wavelength range with a full irradiation intensity of 1.67×10^{-7} Einstein s^{-1} cm^{-2} on the reactor, as determined by ferrioxalate actinometry [22]. The lamp was always switched on at last 30 min before the beginning of the run. The reproducibility of kinetic results was always tested by repeating the runs twice.

3. Results and discussion

3.1. Photocatalysts characterisation

Both FP-made materials consisted of 5–10 nm crystalline micro-aggregates, as revealed by STEM analysis, and possessed equally high surface area (106 m^2 g^{-1}), according to BET analysis. Moreover, as shown by the STEM image in Fig. 2(A), the FP-made Au/TiO_2 sample also displayed the presence of well dispersed, *ca.* 1 nm sized Au nanoparticles, appearing as bright dots deposited over the TiO_2 surface, together with a few bigger (5–6 nm) Au particles. XRD analysis showed that the two FP-made materials also display almost identical crystal phase composition, consisting of *ca.* 90% anatase and 10% rutile, whereas no peaks ascribable to metallic gold could be recognised, as expected, because of the low noble metal loading.

Commercial P25 consists of widely condensed, irregularly shaped, *ca.* 20 nm in size crystalline aggregates, with a 48 m^2 g^{-1} specific surface area (from BET analysis). The HRTEM image of Au/P25 displayed in Fig. 2(B) clearly evidences the presence of *ca.* 2–3 nm sized Au nanoparticles deposited on the P25 surface. According to XRD measurements, the Au/P25 sample displayed the typical mixed phase composition of P25, consisting in *ca.* 80% anatase and 20% rutile. This excludes that the adopted low temperature Au deposition method might induce a marked alteration of the properties of the titania support.

Fig. 3 reports the UV–vis absorption features of the investigated photocatalysts. Both the FP-made and P25 bare TiO_2 materials exhibited a UV–vis adsorption threshold around 400 nm, *i.e.* very close to that of pure anatase. The two gold-containing samples also displayed the plasmonic band in the visible region, typical of gold nanoparticles (<20 nm) [23]. This arises from the collective oscillations of free conduction band electrons, induced by interaction with an incident electromagnetic radiation, whose wavelength far exceeds the particles size. The position, intensity and shape of the plasmonic band depend on several factors, including surface Au particles shape and size [24], Au loading and electronic interactions of gold nanoparticles with the support. In particular, 5–50 nm sized gold nanoparticles exhibit a sharp adsorption band in the 520–530 nm region [15]. For particles bigger than 50 nm the absorption band broadens, extending to all the visible range, whereas for Au particles smaller than 5 nm the band intensity decreases, becoming almost flat for very small particles (<2 nm) [23].

As shown in Fig. 3, the plasmonic band of FP-made Au/TiO_2 is centred at 550 nm, *i.e.* it is red shifted compared to that of colloidal gold (520 nm), indicating the presence of electronic interaction

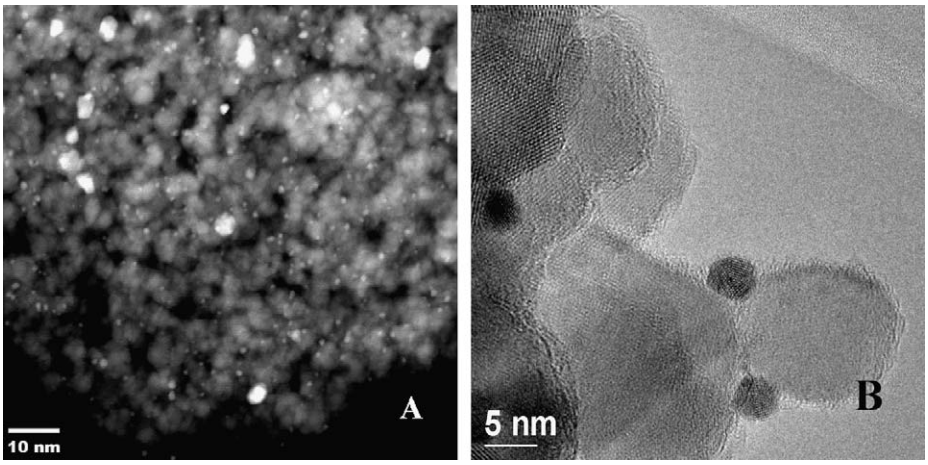

Fig. 2. Left: STEM image of FP-Au/TiO_2. Au nanoparticles appear as bright dots. Right: HRTEM image of Au/P25.

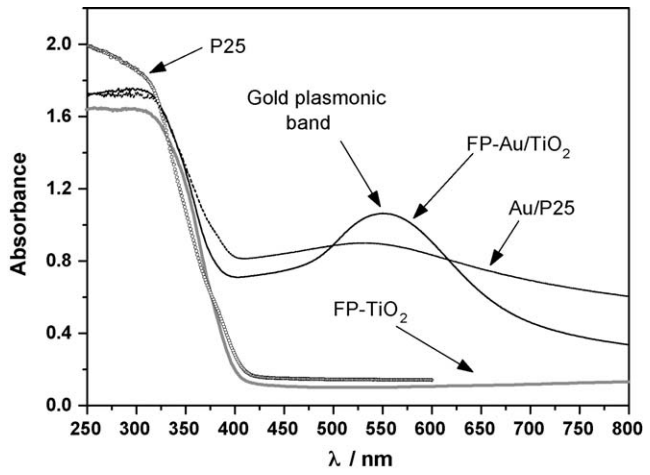

Fig. 3. UV–vis absorption spectra of the investigated TiO_2-based photocatalysts.

between gold and the TiO_2 support. Furthermore, the plasmonic band of FP-Au/TiO_2 was much more intense than that of Au/P25, although the two samples contained the same percent amount of gold. This can reasonably be attributed to the fact that the fraction of 5–6 nm sized Au particles in FP-Au/TiO_2, evidenced by STEM analysis (see Fig. 2(A)), has a major role in visible light absorption, while the contribution of smaller (*ca.* 1 nm) noble metal nanoparticles is expected to be negligible. By contrast, the broad plasmonic band displayed by the Au/P25 sample is in line with the *ca.* 3 nm sized gold nanoparticles deposited on its surface, with a very narrow particles size distribution, as shown by HRTEM analysis (Fig. 2(B)).

3.2. Comparison between the suspension and vapour phase reactors

Hydrogen evolution from the irradiated aqueous suspensions containing a fixed amount of TiO_2-based photocatalysts (*i.e.* 0.3 g L^{-1}, ensuring optimal reaction conditions) occurred at constant rate, depending on the phase composition of the TiO_2 samples [9]. The rate of H_2 evolution, r_{H_2}, was found to increase with increasing the anatase content in FP-made TiO_2-based photocatalysts, pure anatase being the most active one. Furthermore, by properly setting the FP operation parameters, including the selection of the organic solvent/fuel employed in the FP synthesis, the surface area and crystallinity, both key properties of photocatalysts, could be finely tuned up. In particular, FP-made TiO_2 prepared from a xylene solution, ensuring the highest flame temperature during the synthesis, showed even more active than P25 in methanol photoreforming (see Table 1).

Gold addition to both commercial and FP-made TiO_2-based photocatalysts was found to be very beneficial when they were used in the photocatalytic production of hydrogen. Indeed, r_{H_2} increased by one order of magnitude in the photosplitting of pure water [9] and by *ca.* 30 times in methanol photoreforming upon 1% gold addition on TiO_2, attaining a value of 8 mmol of H_2 h^{-1} g_{cat}^{-1}. Gold metal nanoparticles on the semiconductor surface are able to capture photopromoted conduction band electrons [16], thus favouring interface electron transfer and increasing the efficiency of charge separation of the photogenerated electron–hole pairs. However, the addition of noble metal nanoparticles to TiO_2 has been reported to induce controversial effects on the rate of photocatalytic oxidative reactions under aerobic conditions [25–27], when oxygen acts as a conduction band electrons acceptor. The outstanding Au-induced rate increase here observed in hydrogen production thus demonstrates that gold on the semiconductor surface promotes not only charge separation, but also electron transfer to protons adsorbed on the noble metal surface.

When operating with the photocatalyst dispersed in aqueous suspensions, the mass transfer of photoproduced H_2 through the liquid, from the photocatalyst surface to the recirculating gas phase, was found to be rate determining [9]: the hydrogen production rate r_{H_2} almost doubled when the recirculating gas was bubbled into the vigorously stirred suspension, rather than simply flushed in the reactor head space. Furthermore, difficulties were encountered when trying to repeat photocatalytic activity tests employing an already used photocatalyst suspension, because the powder partially deposited from the stirred suspension on the reactor walls during the run, and it could not be totally recovered and separated from the suspension at the end of the run.

The main advantage expected when employing the vapour phase reactor consists in the total elimination of the above-mentioned mass transfer limitations in hydrogen evolution, which in this case occurs directly in the gas phase. Furthermore, the vapour gas cell design ensured a more homogeneous irradiation of the photocatalyst, without any need of stirring to maintain it in the fully illuminated area. Indeed, for all the investigated photocatalysts, the r_{H_2} values attained when an equal amount of powder was dispersed on quartz within the vapour phase cell were at least 30% higher than the r_{H_2} values obtained using the suspension cell, under otherwise identical irradiation conditions (Table 1). The same photoactivity scale was maintained for both bare and gold-bearing TiO_2 samples when employing the two types of cell, with FP-TiO_2 and FP-Au/TiO_2 always performing better than P25 and Au/P25, respectively, and with a *ca.* 30% r_{H_2} increase consequent to gold addition to photocatalysts. Furthermore, fully reproducible photocatalytic activity data were obtained by employing the same photocatalyst bed in up to nine successive 2 h-long cycles, evidencing extremely limited activity losses.

3.3. Identification of intermediate species

During the steam photoreforming reaction, methanol undergoes oxidation, which is expected to proceed through the formation of several intermediates, such as formaldehyde, formic acid and carbon monoxide, up to complete oxidation to carbon dioxide. In order to have a better insight into the possible reaction paths, the composition of the outlet gas from the vapour phase reactor was determined by QMS analysis. The monitored *m*/*z* signals and the corresponding molecular fragments are listed in Table 2.

Table 1
Hydrogen production rate r_{H_2} from methanol photoreforming in the recirculation apparatus using the two setups.

	r_{H_2} (mmol H_2 h^{-1} g_{cat}^{-1})	
	Suspension reactor	Vapour phase reactor
P25	0.16 ± 0.03	0.21 ± 0.02
FP-TiO_2	0.27 ± 0.03	0.46 ± 0.02
Au/P25	5.4 ± 0.3	7.0 ± 0.4
FP-Au/TiO_2	7.9 ± 0.4	10.2 ± 0.5

Table 2
m/*z* signals, and corresponding fragments and species [28], monitored by QMS analysis during the steam photoreforming of methanol over FP-Au/TiO_2 using the vapour phase reactor.

m/*z*	Corresponding fragment	Corresponding species
2	H_2^+	Hydrogen
28	CO^+	Carbon monoxide
29	CHO^+ (aldehydes)	Formaldehyde
31	$CH_2{=}O^+H$ (primary alcohols)	Methanol
44	CO_2^+	Carbon dioxide
45	$^+CO_2H$ (carboxylic acids)	Formic acid

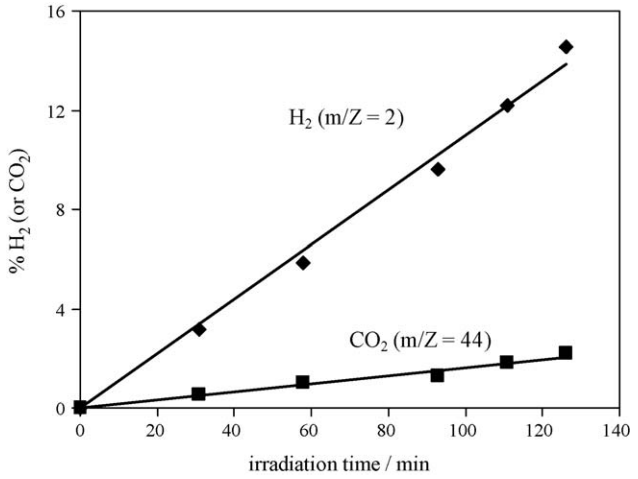

Fig. 4. Percent H_2 and CO_2 amounts in the recirculating gas phase produced from methanol steam photoreforming over FP-Au/TiO_2 using the vapour phase photoreactor setup. Data obtained from QMS analysis.

Fig. 4 displays the concentration profiles of the H_2 and CO_2 percent content in the recirculating gas phase during irradiation of the FP-Au/TiO_2 sample, as obtained by the QMS experiment. Both species evolved at almost constant rate, with $r_{CO_2}/r_{H_2} = 0.08$, which is much smaller than the stoichiometric ratio (1:3) expected from the overall steam photoreforming reaction:

$$CH_3OH + H_2O \xrightarrow{h\nu\,TiO_2} 3H_2 + CO_2$$

This suggests that not all the reacting methanol was oxidised up to CO_2. However, no traces of CO and formic acid were ever detected in the gas phase during the reaction (no peaks were observed on the $m/z = 28$ and $m/z = 45$ QMS signals after recirculating gas injections). This is in full agreement with the results recently published by Wu et al. [8], who also reported that an ultra-low concentration of CO (<5 ppm) is produced during hydrogen evolution from methanol photocatalytic steam reforming on Au/TiO_2 catalyst, with gold nanoparticles smaller than 3 nm. This is an important advantage if the produced hydrogen is to be used to feed a fuel cell, because proton exchange membranes within the fuel cells notoriously undergo severe poisoning by CO.

On the contrary, a relatively high amount of formaldehyde was detected by QMS analysis. The trend of the peak area of the 29 and 31 m/z signals with irradiation time is reported in Fig. 5. In particular, before the beginning of irradiation ($t = 0$), no H_2 ($m/z = 2$) nor CO_2 ($m/z = 44$) could be detected in the CH_3OH/H_2O/He recirculating gas phase in equilibrium with the photocatalyst, and only the signals due to methanol ($m/z = 31$) and water ($m/z = 18$) appeared in the QMS analysis, together with a weak signal at $m/z = 29$ arising form a secondary fragmentation of methanol. During irradiation, the signal of methanol only slightly decreased (indicating a low conversion), whereas the signal at $m/z = 29$, which can unequivocally be attributed to formaldehyde [28], significantly increased with time (Fig. 5).

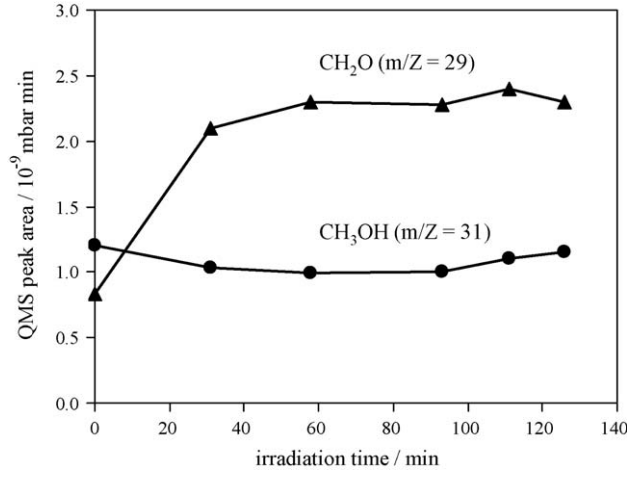

Fig. 5. Time profiles of the QMS peaks areas of the $m/z = 31$ and $m/z = 29$ signals identifying methanol and formaldehyde, respectively.

Formaldehyde can be produced by dehydrogenation of methanol, the first step of methanol oxidation, according to the following reactions:

$$TiO_2 + h\nu \rightarrow h^+_{VB} + e^-_{CB}$$

$$CH_3OH + 2h^+_{VB} \xrightarrow{TiO_2} CH_2O + 2H^+$$

$$2H^+ + 2e^-_{CB} \rightarrow H_2$$

However, while the peak area relative to H_2 and CO_2 constantly increased under irradiation (Fig. 4), indicating the accumulation of these two reaction products in the gas phase, the peak area of formaldehyde remained almost constant during the runs (Fig. 5), *i.e.* there was no evidence of formaldehyde accumulation or subsequent depletion in the gas phase. However, this does not exclude that its overall amount would increase during the runs, as formaldehyde could easily dissolve in the CH_3OH/H_2O liquid solution, when the recirculating gas bubbled through it.

3.4. Selectivity and apparent quantum efficiency

The composition of the $CH_3OH/H_2O/N_2$ (or He) feeding reaction mixture at 912 mm Hg (1.2 bar) total pressure was calculated by considering the gas-phase composition in equilibrium with the CH_3OH/H_2O liquid solution (methanol mole fraction = 0.1) at 30 °C. At this temperature, the vapour pressure of methanol and water are 163.97 and 31.82 mm Hg, respectively. By assuming an ideal behaviour, *i.e.* by applying the Raoult's law, the gas-phase composition is 1.8% CH_3OH/3.14% H_2O/N_2 (or He) balance, corresponding to a H_2O/CH_3OH ratio equal to 1.7.

If we consider that hydrogen is photoproduced only by dehydrogenation of methanol to formaldehyde and by overall steam reforming to CO_2, the selectivity to formaldehyde (S_{CH_2O}) and to CO_2 (S_{CO_2}) can be calculated by the following equations:

$$S_{CH_2O} = \frac{r_{H_2} - 3r_{CO_2}}{r_{H_2}} = 0.76$$

$$S_{CO_2} = 1 - S_{CH_2O} = 0.24$$

Moreover, based on these selectivity values, by taking into account the methanol feeding rate ($\nu_{MeOH} = 43.1\,mL\,CH_3OH\,h^{-1}$) and the H_2 production rate determined by GC ($r_{H_2} = 10.2\,mmol\,H_2\,h^{-1}\,g^{-1}_{cat} = 3.2\,mL\,H_2\,h^{-1}$), one may calculate the conversion of methanol (X_{MeOH}):

$$X_{MeOH} = \frac{r_{H_2}(S_{CH_2O} + S_{CO_2}/3)}{\nu_{MeOH}} \times 100 = 6.2\%$$

Although this value may appear low, it is worth recalling that the unreacted methanol is continuously recovered in the recirculation apparatus and fed again into the reactor. Thus, the almost complete conversion of methanol to CO_2 and H_2 is expected to occur after a sufficient time length.

The apparent photon efficiency of H_2 production (Φ) was finally evaluated, as the ratio between the number of photo-promoted electrons transferred to yield hydrogen per unit time

and the overall number of photons reaching the photocatalyst surface per unit time. The former was deduced from the rate of hydrogen production, as determined by gas chromatographic analysis, r_{H_2}, by taking into account that the transfer of two electrons is required to produce one H_2 molecule; the latter was obtained from the fraction below 400 nm (corresponding to the TiO_2 absorption threshold) of the measured irradiation intensity on the reactor ($I_{\lambda < 400\ nm} = 0.59 \times 10^{-7}$ Einstein s^{-1} cm^{-2}) and the irradiated photoreactor surface area A (20 cm^2). For the best performing FP-Au/TiO_2 photocatalyst we obtained:

$$\Phi = \frac{2 \times r_{H_2}}{I_{\lambda < 400\,nm} A} \times 100 = 6.3\%$$

This relatively high Φ value indicates the use of FP-made Au-containing photocatalysts in the vapour phase as very promising for hydrogen production through steam photoreforming.

4. Conclusions

Flame spray pyrolysis demonstrated to be an effective method for the single step synthesis of very active titania and gold-modified titania photocatalysts for hydrogen production *via* steam photoreforming of methanol. The hydrogen production rate increased up to 30 times upon 1% gold addition on TiO_2. A further *ca.* 30% increase in r_{H_2} was obtained by using the newly set-up vapour phase photoreactor, up to a hydrogen production rate around 10.2 mmol h^{-1} g_{cat}^{-1} (or 71.4 mmol h^{-1} m^{-2}), corresponding to a 6.3% apparent photon efficiency.

On flame-made Au/TiO_2, the first step of methanol steam photoreforming consists in the photocatalytic dehydrogenation of methanol to formaldehyde, the only intermediate species detected in the gas phase. The newly described vapour phase photoreactor proved suitable for testing the same photocatalyst bed in several consecutive cycles, an important improvement with respect to the commonly used suspension photoreactors. This, together with the relatively high photon efficiency here attained, opens the way to the scaling-up of the system.

References

[1] M. Ni, M.K.H. Leung, D.Y.C. Leung, K. Sumathy, Renew. Sustain. Energy Rev. 11 (2007) 401.
[2] E. Selli, G.L. Chiarello, E. Quartarone, P. Mustarelli, I. Rossetti, L. Forni, Chem. Commun. (2007) 5022.
[3] H. Yoshida, K. Hirao, J. Nishimoto, K. Shimura, S. Kato, H. Itoh, T. Hattori, J. Phys. Chem. C 112 (2008) 5542.
[4] G.R. Bamwenda, S. Tsubota, T. Nakamura, M. Haruta, J. Photochem. Photobiol. A: Chem. 89 (1995) 177.
[5] J. Greaves, L. Al-Mazroai, A. Nuhu, P. Davies, M. Bowker, Gold Bull. 39 (2006) 216.
[6] A. Patsoura, D.I. Kondarides, X.E. Verykios, Catal. Today 124 (2007) 94.
[7] A. Sclafani, M.N. Mozzanega, P. Pichat, J. Photochem. Photobiol. A: Chem. 59 (1991) 181.
[8] G. Wu, T. Chen, W. Su, G. Zhou, X. Zong, Z. Lei, C. Li, Int. J. Hydrogen Energy 33 (2008) 1243.
[9] G.L. Chiarello, E. Selli, L. Forni, Appl. Catal. B: Environ. 84 (2008) 332.
[10] Y. Li, G. Lu, S. Li, Appl. Catal. A: Gen. 214 (2001) 179.
[11] Z. Zou, J. Ye, K. Sayama, H. Arawa, J. Photochem. Photobiol. A: Chem. 148 (2002) 65.
[12] R. Abe, M. Higashi, K. Sayama, Y. Abe, H. Sugihara, J. Phys. Chem. B 109 (2005) 16052.
[13] W. Yao, J. Ye, Chem. Phys. Lett. 435 (2007) 96.
[14] H. Kato, A. Kudo, Catal. Today 78 (2003) 561.
[15] A.L. Linsebigler, G. Lu, J.T. Yates, Chem. Rev. 95 (1995) 735.
[16] P. Kamat, J. Phys. Chem. B 106 (2002) 7729.
[17] G.L. Chiarello, I. Rossetti, L. Forni, J. Catal. 236 (2005) 251.
[18] M. Mrowetz, A. Villa, L. Prati, E. Selli, Gold Bull. 40 (2007) 154.
[19] M.D. Advanced Selected Powder Diffraction Data, J.C.P.D.S., Swarthmore, PA, 1974–1992.
[20] H.M. Rietveld, J. Appl. Crystallogr. 2 (1969) 65.
[21] A. Altomare, M.C. Burla, C. Giacovazzo, A. Guagliardi, A.G.G. Moliterni, G. Polidori, R. Rizzi, J. Appl. Crystallogr. 34 (2001) 392.
[22] C.G. Hatchard, C.A. Parker, Proc. Roy. Soc. (London) A235 (1956) 518.
[23] M.M. Alvarez, J.T. Khoury, T.G. Schaaff, M.N. Shafigullin, I. Vezmar, R.L. Whetten, J. Phys. Chem. B 101 (1997) 3706.
[24] U. Kreibig, L. Genzel, Surf. Sci. 156 (1985) 678.
[25] M. Klare, J. Scheen, K. Vogelsang, H. Jacobs, J.A.C. Broekaert, Chemosphere 41 (2000) 353.
[26] B. Sun, A.V. Vorontsov, P.G. Smirniotis, Langmuir 19 (2003) 3152.
[27] H. Einaga, S. Futamura, T. Ibusuki, Environ. Sci. Technol. 35 (2001) 1880.
[28] R.M. Silverstein, F.X. Webster, D. Kiemie, Spectrometric Identification of Organic Compounds, 7th edition, Wiley, Chichester, UK, 2002.